AT622 Section 11
Broadband Infrared Fluxes

The aim of this section is to introduce the more common, approaches to solving broadband infrared radiative transfer. This will culminate in Section 11 in an understanding of the factors that define the long wave radiative heating and cooling in a cloud free atmosphere.

11.1 A Return to the Radiative Transfer Equation

Here we employ the radiative transfer equation developed previously in Section 4 for an absorbing and emitting horizontally stratified atmosphere

$$I(\tau,+\mu) = I(\tau^*,\mu)e^{-(\tau^*-\tau)/\mu} + \int_{\tau}^{\tau^*} B(t)e^{-(t-\tau)/\mu}\frac{dt}{\mu} \tag{11.1a}$$

for $0 < \mu < 1$ which defines radiation that upwells from the atmosphere, and

$$I(\tau,-\mu) = I(0,-\mu)e^{-\tau/|\mu|} + \int_{0}^{\tau^*} B(t)e^{-(\tau-t)/|\mu|)}\frac{dt}{|\mu|} \tag{11.1b}$$

for $0 > \mu > -1$ for downwelling radiation. We now develop this equation in flux form and seek to solve it when it is integrated spectrally.

11.2 Flux Equations and the Infrared Emissivity

It is trivial to transform Eqns. (11.1a) and (11.1b) from an equation of intensity into a radiative transfer equation for flux. First introduce

$$\mathcal{T}(t,\tau,\mu) = \exp[-(t-\tau)/\mu] \rightarrow T^f(t,\tau,\mu) = \exp[-\beta(t-\tau)]$$

where $\beta = 1.66$ is the diffusivity factor, then

$$F_\lambda(\tau) = F_\lambda(\tau^*)\mathcal{T}_\lambda^f(\tau,\tau^*) + \int_{\tau^*}^{\tau} \pi B(t)dT^f(t,\tau)$$

or equivalently

$$\begin{aligned} F_\lambda^+(z) &= F_\lambda^+(z=0)\mathcal{T}^f(0,z) + \int_0^z \pi B_\lambda(z')\frac{d\mathcal{T}^f}{dz'}(z',z)dz' \\ F_\lambda^-(z) &= \int_\infty^z \pi B_\lambda(z')\frac{d\mathcal{T}^f}{dz'}(z,z')dz' \end{aligned} \tag{11.2}$$

Broadband fluxes are then obtained by

$$F^{\pm}(z) = \int_0^{\infty} F_{\lambda}^{\pm}(z) d\lambda \tag{11.3a}$$

In evaluating the fluxes via the radiative transfer equation (11.2) and subsequently integrating these fluxes over the entire IR spectrum, four basic λ scales of dependence need to be resolved (Fig. 11.1)

- slow λ variation of B_{λ}
- the unresolved contour of absorption bands
- line structure, separation, etc.
- the finest scale on which Lambert's Law (and thus on which the RTE) applies.

The usual strategy to accommodate these variations is to:

1. Resolve Planck variation by dividing the spectrum into N discrete intervals (typically ranging from 4-20 intervals). Models at this resolution are referred to as coarse or wide band models).

2. Develop a model of the transmission function for each of these intervals. This can be done using a band model or the *k*-distribution model of transmission

3. The broadband fluxes are then obtained for example by summing over all N intervals, namely

$$F \approx \sum_{i}^{N} F_i \Delta\lambda_i \tag{11.3b}$$

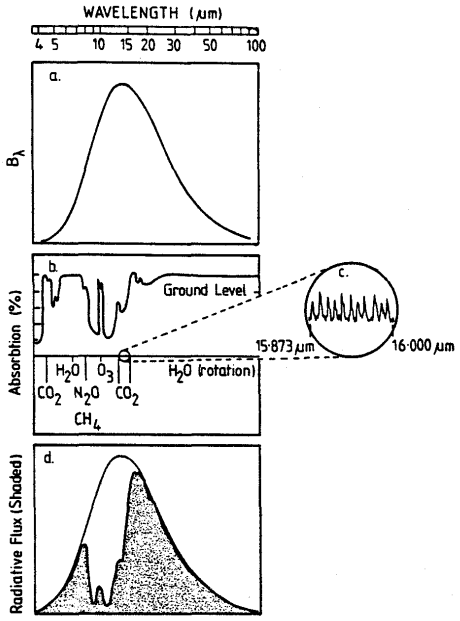

Fig. 11.1 Schematic of the various frequency scales encountered in the calculation of atmospheric longwave flux. These scales refer to (a) the Planck curve, (b) atmospheric gaseous absorption spectrum for longwave radiation reaching the ground, (c) higher resolution spectral absorption highlighting individual lines and line separations, and (d) the convolution of the absorption spectrum and the Planck function to give atmospheric flux (shaded area).

(a) Emissivity Approaches

Obviously the problem of calculating flux can be significantly simplified by keeping the number of spectral intervals to a minimum. An approach designed to do this is the emissivity method, which in principle seeks to reduce N $\rightarrow$ 1.

If we note that

$$\mathcal{T}_\lambda^f(z,z') = 1 - A_\lambda(z,z')$$

then

$$F^+(z) = \int_0^\infty \pi B_\lambda(z)[1 - A_\lambda(0,z)]d\lambda + \int_0^\infty d\lambda \int_z^0 \pi B_\lambda(z') \frac{dA_\lambda}{dz'}(z,z')dz'$$

$$F^-(z) = \int_0^\infty d\lambda \int_z^\infty \pi B_\lambda(z') \frac{dA_\lambda}{dz'}(z,z')dz'$$

Define

$$\varepsilon(z,z') = \frac{1}{\sigma T^4} \int_0^\infty A_\lambda(z,z')\pi B_\lambda(T)d\lambda$$

as the "emissivity" (note this is a function of temperature in principle), then

$$\begin{aligned} F^+(z) &= \sigma T_g^4(1 - \varepsilon(0,z)) + \int_z^0 \sigma T^4(z') \frac{d\varepsilon}{dz'}(z',z)dz' \\ F^-(z) &= \int_z^\infty \frac{d\varepsilon}{dz'}(z,z')\sigma T^4(z')dz' \end{aligned} \tag{11.4}$$

The approach is then to estimate the value of the absorption path u defined along the path (z, z') and deduce the value of ε from an *a priori* relationship between ε and u. Examples of such relationships are given in Figs. 11.2a and 11.2b. The latter shows the emissivity for three broad spectral regions and indicates how the temperature dependence reverses from one region to another to produce a much weaker dependence on the broadband emissivity.

(b) Illustrating the Emissivity Approach

Consider an n-layer atmosphere as shown in Fig. 11.3. Suppose we require to calculate the up- and downwelling broadband fluxes at some level between layer m and m + 1 (i.e., at level m + 1). For illustration, consider the contributions to the upwelling flux by the ℓ^{th} layer as illustrated. In calculating this contribution, we consider two basic approaches;

- Use Eqn. (11.1). The first step is to establish the path length. For example, the path length extending from level ℓ to level m + 1 is

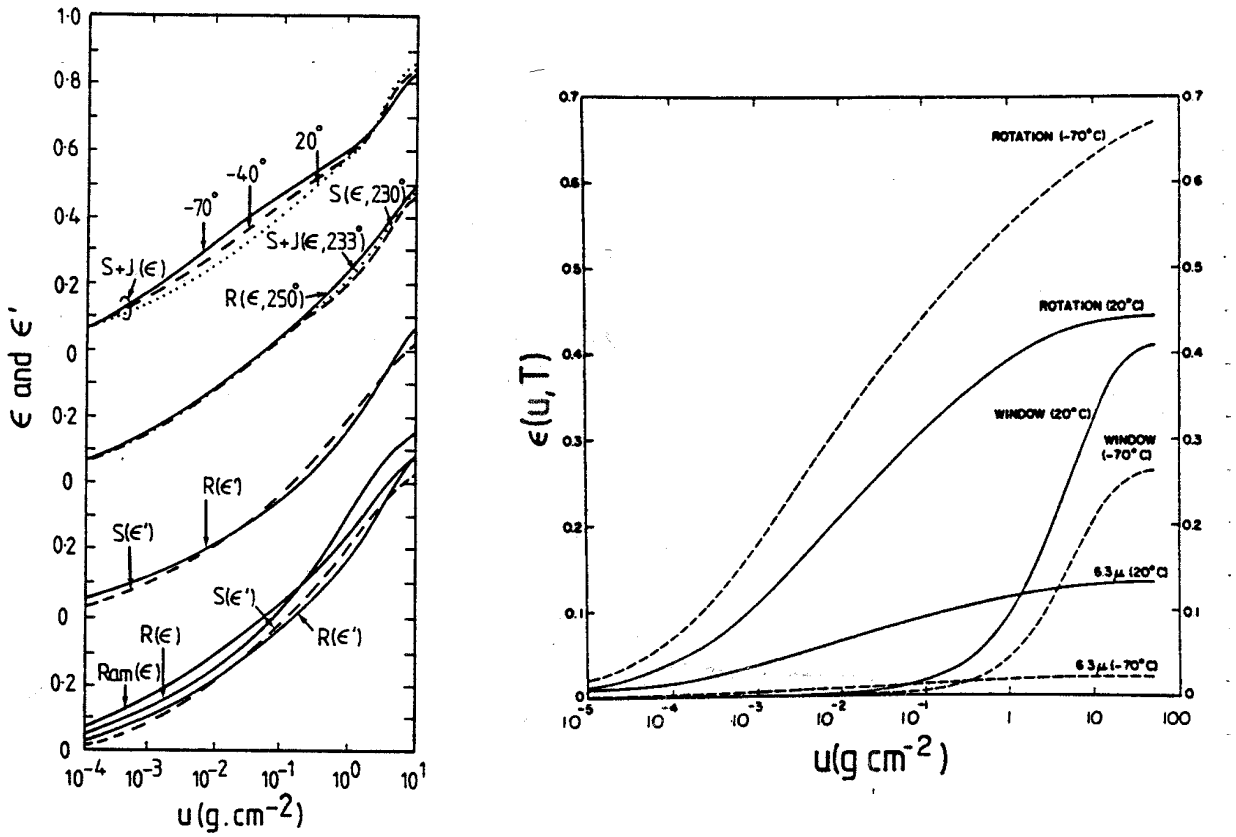

Fig. 11.2 (a) The emissivity ε and the modified emissivity ε′ as a function of water vapor path u. These relationships are taken from a variety of sources. R. Rodgers (1967), S. and J. Staley and Jurica (1970), RAM-Ramanathan et al. (1983), S. Sasamori (1969). The upper curves show ε for three different temperatures and the lower curves show comparisons of ε and ε′. (b) The contributions to the total water vapor gray body emissivity by three broad spectral regions, which include the water vapor rotation band, 6.3 μm band and the atmospheric window (excluding e-type absorption). These contributions are shown as a function of u (of $\bar{u}$ as the case may be) for two different temperatures (from Staley and Jurica, 1970).

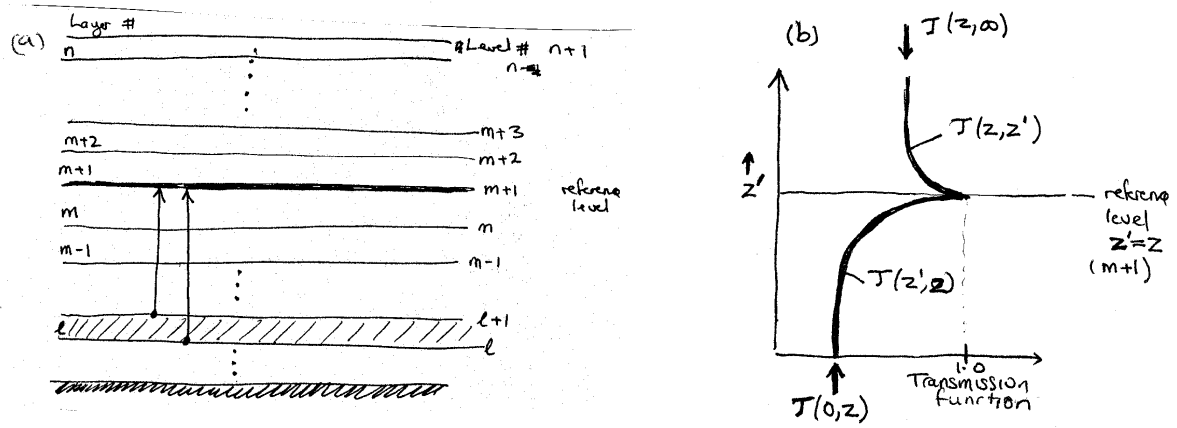

Fig. 11.3 (a) An illustration of an emissivity flux calculation. (b) The cusp in the transmission function with a discontinuity at level m + 1.

$$u_+ = u(\ell)\left(\frac{\overline{p}(\ell)}{p_o}\right)^n + u_-$$

where

$$u_- = u(\ell+1)\left(\frac{\overline{p}(\ell+1)}{p_o}\right)^n + \ldots + u(m)\left(\frac{\overline{p}(m)}{p_o}\right)^n$$

where the overbar on pressure denotes the layer average, and the power n is the scaling factor (note we again neglect temperature here for simplicity). The contribution to the broadband upwelling flux at $m + 1$ by the ℓ^{th} layer is

$$\Delta F^+(m+1,\ell) = \sigma\overline{T}^4(\ell)[\varepsilon(u_+) - \varepsilon(u_-)]$$

and the total flux follows as

$$F^+(m+1) = \sum_{\ell=1}^{m} \Delta F^\dagger(m+1,\ell)$$

- An alternative approach is to integrate Eqn. (11.1) by parts to obtain

$$\begin{aligned} F^+(z) &= \sigma T_g^4 + \varepsilon(0,z)(\sigma T_+^4 - \sigma T_g^4) + \int_0^z \varepsilon(z',z)\frac{d\sigma T^4(z')}{dz'}dz' \\ F^-(z) &= \sigma T_\infty^4(1-\varepsilon(z,\infty)) + \int_\infty^z e(z,z')\frac{d\sigma T^4(z')}{dz'}dz' \end{aligned} \qquad (11.5)$$

where T_∞ is usually set to zero and where T_+ is the air temperature just above the surface (and allows for a temperature jump there). The contribution to the flux at $m + 1$ is thus

$$\Delta F^\dagger(m+1,\ell) = \varepsilon(u)[\sigma T^4(\ell-1) - \sigma T^4(\ell)]$$

where u is the scaled path extending from the mid-point of the ℓ^{th} layer to the $m + 1$ level. This is usually the preferable way to evaluate the integral term as $\Delta\sigma T^4$ is known more accurately in principle than is $\Delta\varepsilon$ (i.e., this implies that the temperature variation with z is better known than is the variation of q with z).

There are two important issues to bear in mind in performing these calculations. First, calculation of the flux at each level requires the evaluation of the transmissivity/emissivity for all n levels. Thus the computation of the flux profile therefore goes as n^2. The second point is that no matter which approach is taken, the integration through the adjacent most layer (i.e., the m^{th} layer for the example considered here for upwelling radiation) should be performed by dividing the layer into sublayers to resolve the cusp (Fig. 11.3a) in the transmission function (note that $\mathcal{T}(z, z') = 1 - \varepsilon(z, z')$). Both issues pertain to band model schemes as well as emissivity schemes.

Example 11.1. The emissivity of the atmosphere. Consider a single isothermal layer atmosphere of temperature T_1 overlying a black surface radiating at a temperature T_g. The temperature of this surface is maintained through absorption of solar radiation by an amount $Q_o(1 - \alpha)/4$ and the atmosphere is transparent to this radiation. Assuming the atmosphere, planet, and surface are in radiative equilibrium, we seek to estimate the emissivity of the atmosphere and T_1 that give rise to the T_g = 288 K for Q_o = 1370 Wm^{-2} and α = 0.3.

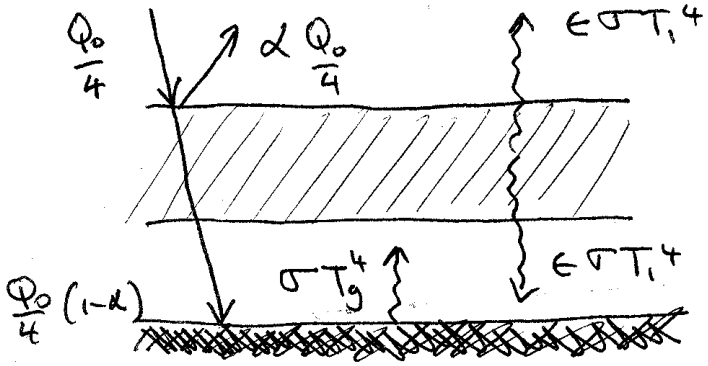

From Eqn. (11.1) it follows that the outgoing longwave radiation at the top of the atmosphere simplifies to

$$F^+(z=\infty) = \sigma T_g^4 (1 - \varepsilon(0,\infty)) + \varepsilon(0,\infty)\sigma T_1^4$$

and the radiative equilibrium condition at the top of the atmosphere is

$$\frac{Q_\odot(1-\alpha)}{4} = \sigma T_g^4 (1-\varepsilon) + \sigma T_1^4 \varepsilon$$

where we simply write ε for $\varepsilon(0,\infty)$. The equilibrium condition for the atmosphere is

$$T_g^4 = 2T_1^4$$

and it follows that T_1 = 242 K for T_g = 288 K. The equilibrium at the surface is

$$\frac{Q_\odot(1-\alpha)}{4} + \varepsilon\sigma T_1^4 = \sigma T_g^4$$

where the second term of the left-hand side is the atmospheric emission to the surface. Rearrangement gives

$$\varepsilon = 2\left[1 - \frac{Q_\odot(1-\alpha)}{4\sigma T_g^4}\right]$$

and a value ε = 0.78 [Compare this with the value you estimate from Fig. 11.2 assuming 2.8 gm^{-2} for a global mean value of u.]

(a) Overlapping Gases in the Emissivity Approach

REF: Staley and Jurica, 1970: *J. Appl. Met.* When two overlapping gases, such as CO_2 and H_2O, absorb in the same spectral region, the combined transmission may be written as the product

$$\mathcal{T}_{over} = \mathcal{T}_{CO_2} \times \mathcal{T}_{H_2O}$$

provided the transmission function for each species is of a pure exponential form (as applies to the random band model). For broadband emissivity,

$$\mathcal{T} = 1 - \varepsilon$$

and, since ε is not a simple exponential function of path u (c.f., Fig. 11.2), the following is NOT true

$$T_{over} = [1 - \varepsilon(u_{H_2O})] \times [1 - \varepsilon(u_{CO_2})].$$

An approach to treat this type of overlap in the framework of emissivity models is to define the emissivity of the combined path

$$\varepsilon(u_{H_2O} + u_{CO_2}) = \varepsilon(u_{H_2O}) + \varepsilon(u_{CO_2}) - \Delta\varepsilon(u_{H_2O}, u_{CO_2})$$

where $\Delta\varepsilon$ is an overlap correction factor.

11.3 Intercomparison of Different Methods and Some Selected Results

Performances of both emissivity and coarse band models were tested as part of an international intercomparison program, the Intercomparison of Radiation Codes for Climate Models (ICRCCM). The results of these intercomparisons are summarized in a special issue of *J. Geophys. Res.,* **96**, D5, 1991.

(a) Features of the Clear-Sky Results (Ellingson, et al. 1991)

The range of in-model flux calculations and the manner by which these have changed over the course of ICRCCM is given in Fig. 11.4a through a comparison of the 1984 (open) and 1988 (shaded) distributions of downward fluxes at the surface relative to line-by-line calculations. The LBL calculations are from the Fels-Schwarzkopf (GFDL) model, and the MLS profile with all of the constituents (i.e., H_2O, O_3, and 300 ppmv CO_2) was used as input to all models. For this case, the 1988 data show nine more non-LBL models that agree to within ±2% of the GFDL LBL results, seven of these being from new participants. Of the 22 climate model type calculations for this case, 13 are within the ±2% range, and all but one fall within the ±6% range. On a percentage basis, 67% of the 1998 non-LBL model results agree to within ±2% of the LBL results as compared with 58% in 1984. Similar results hold for the net flux comparisons at the tropopause and the upward flux at the top of the atmosphere for this atmospheric profile.

The increase in the fraction of models agreeing closer with the LBL results also holds for the change of the net flux between the surface and tropopause (13 km), denoted ΔF_{net}, as illustrated in Figure. 11.4b. The 1988 data find more than twice the number of models agreeing with the LBL results to within ±2% than the 1984 data. About 82% of the 1988 and 75% of the 1984 model data agree with the LBL results when the range for agreement is increased to ±6%, or a rate of temperature change of about ±0.1 K/d.

However, only 60% of the climate model type calculations fall within this ±6% range. It should be noted that comparisons of vertical profiles of flux divergence have not been examined in detail, but our experience with the 1984 data suggest that much larger differences than those noted above will be found in some layers.

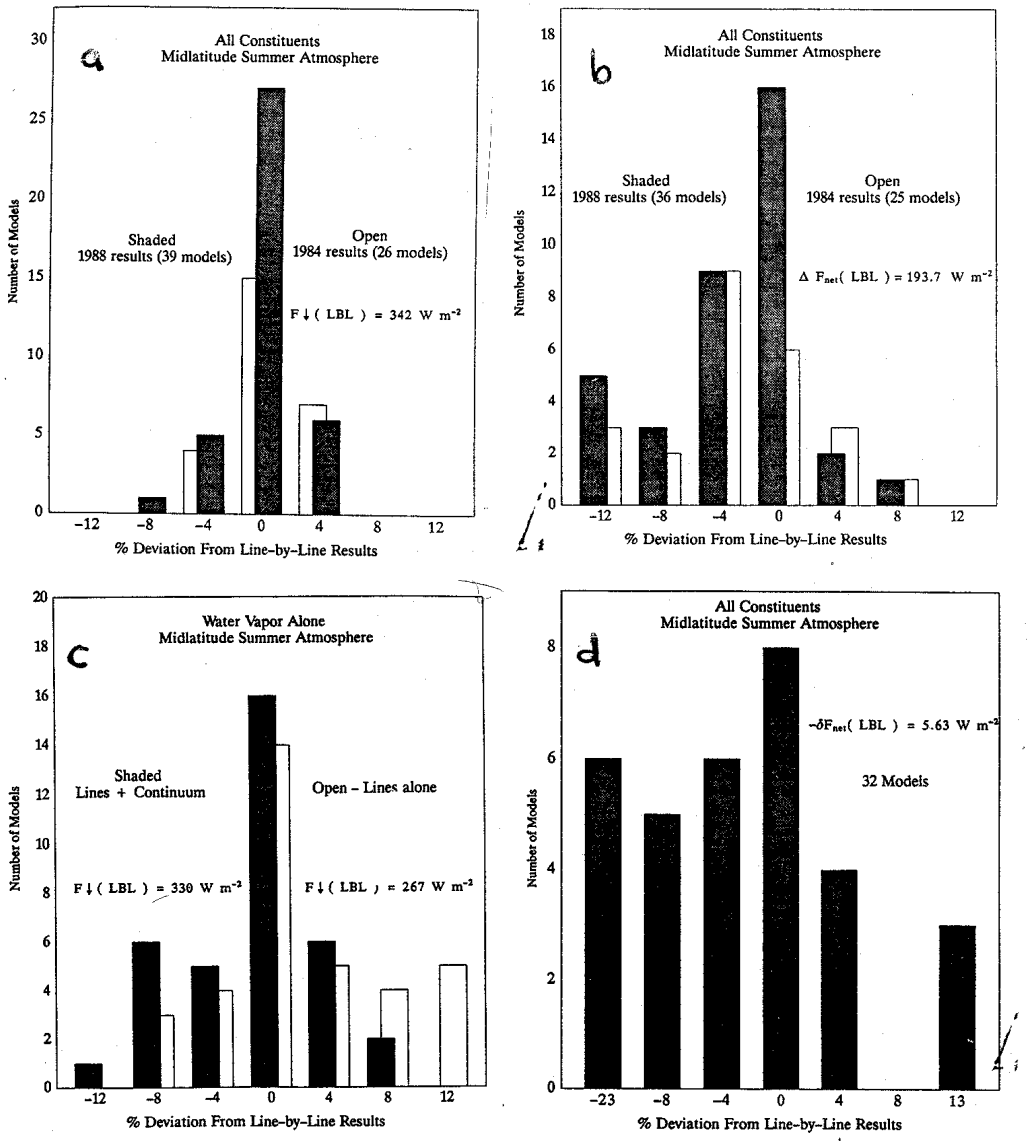

Fig. 11.4 (a) Comparison of 1984 (open) and 1988 (shaded) distributions of downward fluxes relative to a LBL calculation. (b) The flux divergence of the troposphere (0-13) km. (c) The 1988 distributions of downward flux differences relative to a LBL result with vaporlines only (open) and lines plus continuum (shaded). (d) Change in the net flux at the tropospause after doubling CO_2 from 300 ppmv relative to the LBL calculation.

Although Fig. 11.4a and b give some confidence in the general ability of the less detailed models to reproduce the gross features of the line-by-line results, this confidence is shaken somewhat when we examine the results when H_2O is the only absorbing gas as shown in Fig. 11.4c. When only the local lines of H_2O are included in the downward flux calculations more than half of the results are outside of the ±2% range, which was also seen in the 1984 data (not shown). The continuum masks many of the very

large positive differences, but it also amplifies many of the large negative ones. In general, the effect of the continuum and the overlap of different species tends to mask many of the large differences between absorption parameterizations of individual gases. Although this masking reduces the range of flux values expected from absorption differences alone, it also prohibits extending the range of agreement of this study to significantly different atmospheric conditions.

One of the major areas of study for ICRCCM was the sensitivity to changes in the concentration of the major absorbers, particularly CO_2. An important quantity calculated in CO_2 doubling studies is the change in the net flux at the tropopause as CO_2 doubles, denoted as δF_{net}. Figure 11.4d shows the distribution of δF_{net} relative to the LBL calculations clear-sky MLS conditions. The LBL models agree on this result to about ±1% of 5.6 Wm^{-2}. However, the various band model results differ by up to 50% of this value. Of the 17 codes actually used in climate models, six fall within ±5% of the LBL results, and one differs by more than 25%. The close agreement with LBL results for some of these models is not surprising because of tuning.

11.4 Flux Profiles

Figure 11.5a shows the vertical profile of the change in net upward longwave, net downward shortwave and total flux due to doubling the amount of CO_2. The solar flux change ΔS is negative due to enhanced absorption by CO_2, and the longwave flux change ΔF is positive indicating enhanced emission of approximately 1 Wm^{-2}.

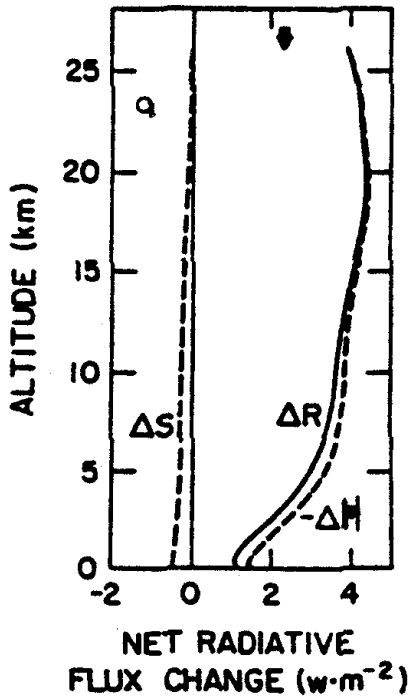

Fig. 11.5 Effect of CO_2 doubling on net radiative fluxes at 30°N. S is the net downward solar flux, F the net upward IR flux, and $R = S - F$ is the net downward radiative flux. The symbol Δ preceding a quantity denotes a change in the flux due to doubling of CO_2. The arrow indicates the value at the top of the atmosphere for ΔR.

11.5 TOA Clear Sky Longwave Fluxes

Slingo and Webb (1992) apply a 10 cm^{-1} band model, together with data from the operational archive at the European Centre for Medium Range Weather Forecasts (ECMWF) to simulate the clear sky o1r. Temperature and specific humidity data on 19 model levels were directly incorporated into the simulations along with analyzed surface pressure. The radiation model is constructed around a high spectral resolution radiative transfer model (Shine, 1991) that incorporates the ECMWF analyses from the operational archive. The accuracy of the radiation model employed by SAMSON was checked using a single column version applied to ICRCCM test profiles (Ellingson et al., 1991). Calculations of clear sky outgoing longwave radiation (hereafter represented as F_∞) for five standard atmospheres with effects of water vapor, carbon dioxide, and ozone differed from line-by-line calculations of F_∞ by approximately 1 Wm^{-2} suggesting excellent agreement with these reference calculations (Slingo and Webb, 1992). Comparison of clear sky values of F_g depend to a small extent an the specific details of how the continuum absorption is dealt with in the model. The treatment of the continuum is described by Shine (1991) and is based on the far wing treatment of Clough et al., (1986). Variations of the treatment of this continuum can introduce uncertainties in calculations of the surface flux up to 10 Wm^{-2} (Ellingson et al., 1991). SAMSON simulations of F_g agreed with reference ICRCCM calculations of this flux within 3 Wm^{-2}.

Simulations of the monthly mean clear sky fluxes over the ice-free oceans were carried out for the period March 1989 to February 1989, which is also a period for which both ERBE and SSM/I observations are available. As in the original Study of Slingo and Webb (1992), these simulations apply to a horizontal resolution of 5 degrees. The radiation code applied to each daily analyses (a mean of four 6-hourly analyses for each day) and then averaged to produce the monthly mean flux distributions, which are used in the analyses described below. Both Slingo and Webb (1992) and Webb et al. (1993) discuss the differences between the simulated fluxes from SAMSON and the clear-sky values of F_∞ obtained from ERBE. Figure 11.6a presents examples of scatter diagrams of the SAMSON F_∞ versus the ERBE F_∞ for April, July and September 1988 and January 1989 to highlight some gross features of these comparisons. For instance, a slight positive bias of 3-5 Wm^{-2} exists between the SAMSON and ERBE fluxes, a bias similar in both sign and magnitude to that of the ERBE clear sky flux data (Harrison et al. 1988). As Webb et al. (1993) show, there are regions (not shown) where the differences between the simulated fluxes and ERBE derived fluxes exceed this small bias, such as over the areas of marine boundary layer clouds off the west coasts of the major continents where differences may be as large as 10 Wm^{-2} (Fig. 11.6b). These areas can be traced to biases in the ECMWF water vapor data (e.g. Liu et al., 1992; Stephens and Jackson, 1994) as highlighted in the difference between TOVS and SSMI column water vapor.

11.6 Longwave Fluxes at the Surface - A Satellite Retrieval

In Section 4, we derived a relationship between the longwave flux to the surface and the OLR (Eqn. (4.16c)). With arguments similar to those introduced in Section 6.2(b), we introduce the relationship (rearrangement of Eqn. (4.16c)),

$$\mathcal{F} = \frac{F_g}{F_\infty} = b\tau_s \tag{11.6}$$

and suppose that a simple relation exists between $\mathcal{F}$ and precipitable water w of the form

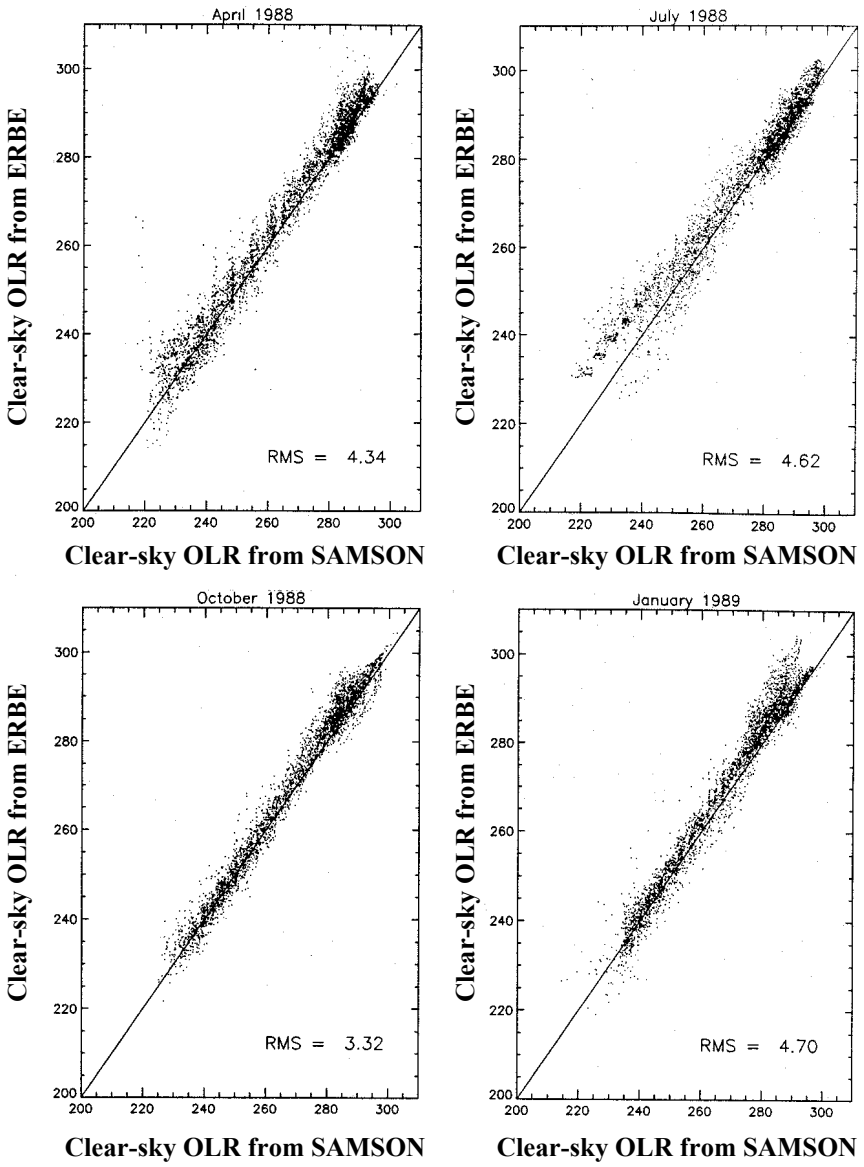

Fig. 11.6 (a) Scatter diagrams of SAMSON simulated F_∞ versus ERBE analyses of clear-sky longwave fluxes for April, July and September, 1988, and January 1989. (b) Comparison of the OLR difference between ERBE and the ECMWF simulation (upper) and the TOVS precipitable water and SSM/I precipitable water (lower).

$$\mathcal{F} = a_2 + c_2 w \tag{11.7}$$

in an entirely analogous way to Eqn. (6.5) where a_2 = 0.937 and c_2 = 0.0102 $kg^{-1}m^2$**.** Unfortunately, we do not have global observations of F_g and thus we cannot derive $\mathcal{F}$ solely from independent observations to test this relationship. The relationship between predicted fluxes and w is shown in Fig. 11.7

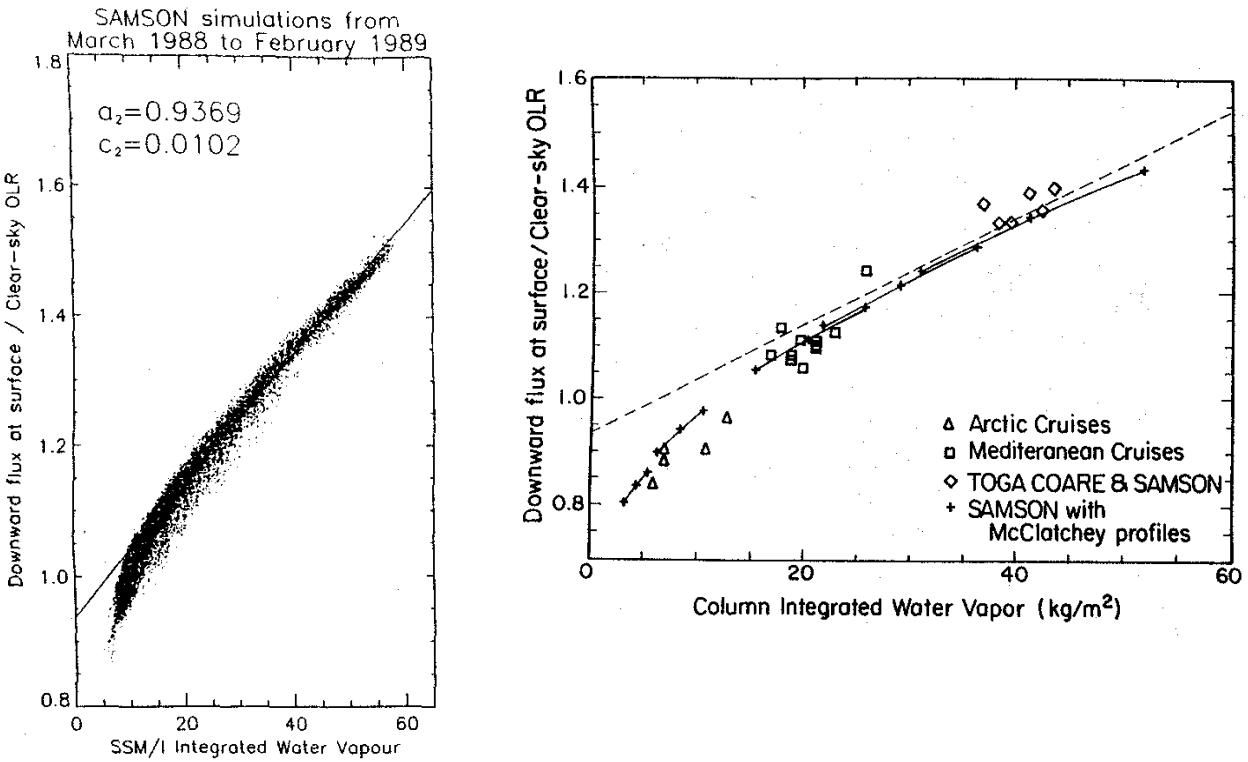

Fig. 11.7 The flux ratio $\mathcal{F}$ derived from combined simulations of January and July fluxes as a function of w.

Except for particular regions, the simulations of clear sky F_∞ from SAMSON generally agree with ERBE estimates of this flux to within 5-10 Wm^{-2}, which is considered to be of the same order of uncertainty as the latter. There are also no *a priori* reasons to expect the simulations of clear-sky F_g to be grossly in error although how the specific details of how the continuum absorption is modeled may introduce an uncertainty of the order of 10 Wm^{-2}. Bearing this possibility in mind, simulated distributions of F_g over the ice-free oceans are presented in Figs. 11.8a and b in the form of the surface net flux (i.e., $\sigma T_s^4 - F_g$ F,,). The distributions in Figs. 11.8c and d were derived from satellite distributions of *w* and OLR and the specified relationship that best fits the data in Fig. 11.7. The maps of the surface net flux derived by this approach and are presented here for comparison with actual model simulations shown in Figs. 11.8a, and b and match the simulations to ±6 Wm^{-2}.

The smallest net fluxes of around 40-50 Wm^{-2} occur in the tropical convergence zones over the Pacific and Indian Oceans and in the Northwest Pacific in July. A significant annual variation close to the northern continents also appears to exist which is associated with changes in the atmospheric circulation associated with the summer and winter monsoons.

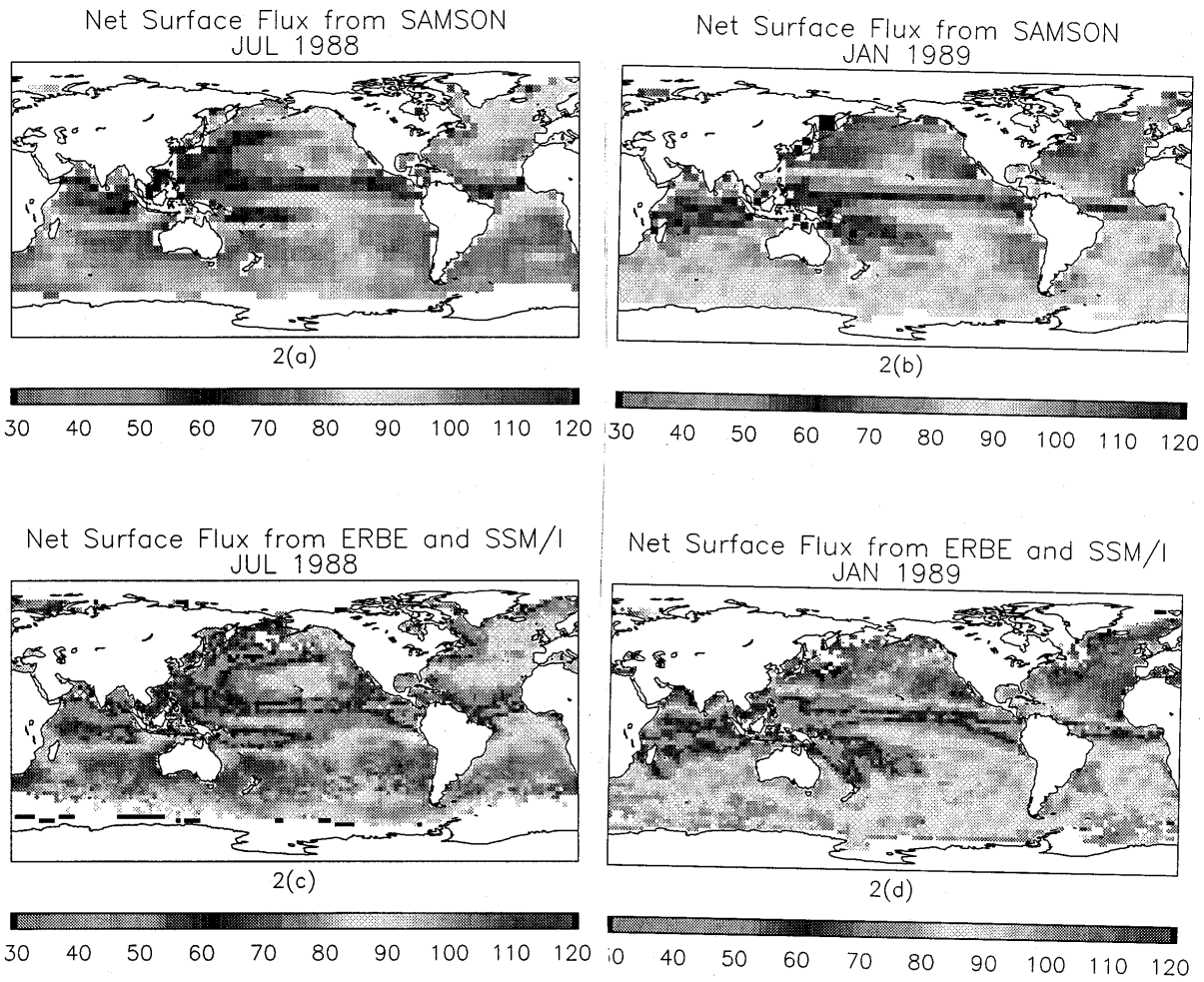

Fig. 11.8 (a) and (b) are distributions over the oceans of the July and January SAMSON simulations of surface net longwave flux. (c) and (d) are the same as (a) and (b) but the net flux is deduced using a linear regression of the flux ratio, ERBE air and SSM/I precipitable water.